Processing and characterization of textured mullite ceramics from phyllosilicates

S. Deniel [a], N. Tessier-Doyen [a], C. Dublanche-Tixier [b], D. Chateigner [c], P. Blanchart [a],*

[a] *Laboratoire GEMH, ENSCI, 47 à 73, avenue Albert Thomas, 87065 Limoges Cedex, France*
[b] *SPCTS UMR CNRS 6638, Université de Limoges ENSIL, 87068 Limoges Cedex, France*
[c] *CRISMAT-ENSICAEN-IUT-Caen, Université de Caen Basse Normandie, 14050 Caen, France*

Abstract

Ceramics are obtained from a kaolinite aqueous suspension and are shaped by centrifugation. It favors preferred orientations of particles in the powder compact. Sintered samples at 1410 °C were analyzed by QTA and SEM to determine mullite orientation and the important role of process parameters in the organization degree is evidenced. The *c*-axes of mullite are mainly aligned parallel, but randomly in the sample plane to form a planar texture. A second texture component is seen with *b*-axes oriented parallel to the centrifugation direction.

Mechanical properties are closely related to the organization degree of mullite crystals that is consistent with the development of an interconnected mullite network within the microstructure. At the microscopic scale, Young's modulus values determined by nano-indentation and by ultrasonic immersion techniques in directions parallel and perpendicular to layers evidence an anisotropic behavior of samples. The specific and important role of residual porosity is also shown with the comparison of mechanical behavior of different centrifuged samples.
© 2010 Elsevier Ltd. All rights reserved.

Keywords: Mullite; Centrifugation; Pole figures (QTA); Nano-indentation; Fracture strength

1. Introduction

Ceramics with highly organized microstructures exhibit improved mechanical properties[1–3] such as flexural strength, fracture toughness, hardness and Young's modulus. Some ceramic processing techniques are able to spatially control the microstructure and induce the development of organized microstructures during sintering.[4,5] The morphology, periodicity, and connectivity of crystals in microstructures are fundamental parameters to improve applications under severe conditions as for alumina[6,7] mica composites,[8,9] tungsten carbide,[10] supraconductors[11] or piezoelectric ceramics.[12]

In clay-derived ceramics, mullite crystallization depends on the used clay minerals and on interaction with other components. Using kaolinite, solid-state reaction ensures slow crystallization and growth of crystals.[13] With mica minerals like illite, the alkali-silicate liquid favors crystal growth, but the reaction path is not the same as from kaolinite.[14] In other clay minerals or mixed clay minerals, the alkali, Fe or other impurities change the liquid composition and its behavior that influence recrystallization mechanisms.

Mullite quantity and size depend not only on firing time and temperature, but also on the quantity of liquid and its composition at high temperature, which in turn depends on feldspars and other flux as Fe impurities.[15,16] The shape of mullite crystals is always elongated. While small (10–50 nm) rod-like crystals form at lowest temperatures, larger (3–15 μm) acicular crystals are generally observed at highest temperature ranges. Mullite stoichiometry evolves gradually as a function of starting composition, reaction time and temperature. The Al/Si ratio is close to 2:1 in primarily crystallized mullite and changes continuously to 3:2 at larger forming temperatures. This behavior is due to the silicate liquid, in contact to already formed mullite crystals. Large alkali contents of the liquid result in a low viscosity, which enhances crystal growth. But silicoaluminate ceramics are more or less heterogeneous at the grain scale and mullite recrystallization depends on the locally available liquid and solid particles so that the system is not at equilibrium resulting in a large distribution of mullite size and stoichiometry.

As mullite size, shape and content change with temperature,[17] the role of the interlocking mullite network changes and exhibits an effect on the macroscopic strength. The reinforcement of materials can be explained within the hypothesis that the difference in thermal expansion coefficients between the matrix glassy phase and the dispersed particles, such as quartz and mullite,[18] produces a compressive stress on the glassy phase.[19] In a different approach, the high mechanical properties are attributed to the formation of a micro-composite microstructure where elongated mullite crystals and remaining crystals from the starting composition are embedded in the glassy matrix.[20] It induces the deflection of the crack path along the particle–matrix interfaces.

The fracture behavior depends also on porosity. Pore shapes and distribution within the material change the local bulk density.[21,22] The porous structure of fired ceramics is firstly determined by the microstructure of the green body. This phenomenon explains why highly improved compaction methods are often used to optimize the grain-packing during shaping.[23]

Due to heterogeneities, mechanical behaviors are dependent on the measurement location, since they are related to the local microstructure and the volume involved by measurements.[24] When indentation measurements are operated out with different notch depths, the local strain or cracks evolve through zones having different microstructures.[25] The macroscopic behaviors are related to subcritical growth of cracks in the material at heterogeneous interfaces.

The objective of this study is to obtain silicate ceramics with improved mechanical properties. Materials are shaped by centrifugation of a concentrated aqueous suspension of a kaolin powder. The sintering and centrifugation parameters have been optimized to favor the formation of an organized microstructure with mullite. Mechanical properties at microscopic and macroscopic scales have been also characterized and correlated with microstructural characteristics, mullite crystallite orientation and material porosity.

2. Experimental procedure

Kaolin (BiP Kaolin, Denain-Anzin-Minéraux) suspensions were prepared by grinding kaolin particles in water with a dispersant (Dolaflux, 0.2 wt%) in a planetary mill (Fritsch, Pulverisette, 40 min, 180 rpm). The suspensions were placed in a cylindrical container to operate centrifugation. The container axis, r, was placed perpendicular to the centrifugation axis, z, resulting in disc-shaped samples (diam. 36 mm, height 1–5 mm) having their revolution axis perpendicular to the axis of rotation of the centrifugation apparatus (Sigma 301). Centrifugation was operated up to obtain density equilibrium, defined by a constant thickness of the powder compact.

Experiments were performed with a suspension height in the container in the range 8.4–14.9 mm. Centrifugation needs three successive stages: (1) centrifuging at 3000 rpm during 20 min; (2) removing the excess of water and (3) centrifuging at 3600 rpm during 10 min.

During the process, the equilibrium state of the powder compact results from the settling of the suspensions. The mean compressive pressure P_m applied onto the centrifuged powder compact was described as a power-law function of the average density d_m.[26,27]

$$P_m = \beta d_m^n \tag{1}$$

where P_m is a function of the apparatus size, rotation speed and suspension height in the container. The n and β parameters depend on the suspension rheology, mean density and characteristics of particles. The possible occurrence of aggregated particles can also influence the density of the powder compact.[26] During centrifugation, the solid content of the liquid decreases with time and the maximum pressure stress is attained at the bottom of the container at time $t = 0$. At equilibrium, the density of the top layer of the powder compact tends to that of the liquid. The density profile $d(r)$ of the powder compact was described as[26]:

$$\frac{d(r)}{d_{max}} = \left(1 - \frac{r}{r_{max}}\right)^{1/(k-1)} \tag{2}$$

where d_{max} is the density of the bottom layer of the powder compact. This equation evidences that the exponent k of the power law in the pressure–density relationship is a critical parameter, which changes the $d(r)/d_{max}$ curve profile.

After centrifugation, raw disks were dried between two flat porous materials to ensure a good flatness. Sintering was operated at 5 °C/min heating rate and the maximum temperature of 1410 °C was maintained during 2 h. The value of maximum temperature was optimized as a function of mullite recrystallization process, during preliminary experiments.

To characterize crystal orientation, quantitative texture analysis (QTA) was performed using a 4-circle diffractometer allowing rapid acquisition of the whole diffraction pattern up to 80° 2θ, for each tilt angle χ and azimuth angle φ of the orientation of samples. Diagrams were acquired for many sample orientations (using a 5° × 5°) measuring grid in (χ, φ up to $\chi = 55°$). The whole dataset was analyzed using whole-powder-pattern Rietveld analysis within the combined analysis formalism,[28] in which the orientation distribution function was refined using the E-WIMV approach.[29] Pole figures were plotted using an equal area projection on the disc plane, with their center being the r direction and are normalized into distribution densities using multiple of a random distribution (m.r.d.) units.

Using such units, a sample without texture exhibits homogeneous pole figures with 1 m.r.d. values, while a textured sample shows minima and maxima in the pole figures ranging from 0 m.r.d. (absence of crystals oriented in this direction) to infinity (for a single crystal in few directions). The overall texture strength is evaluated through the texture index.[28] The normalization of the pole figures into m.r.d. values is operated during the orientation distribution (ODF) refinement of crystallites during the E-WIMV step. The ODF and profile refinement reliabilities are estimated using conventional reliability factors.[30]

The determination of elastic properties was carried out by nano-indentation method (NanoXP™, MTS Instruments) with a Berkovich tip, in continuous stiffness measurement mode (CSM).[31,32] Two penetration depths were used: 100 nm to deter-
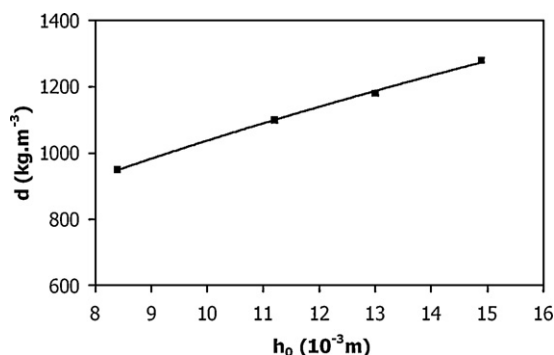
Fig. 1. Density of the powder compact as a function of the suspension height after centrifugation.
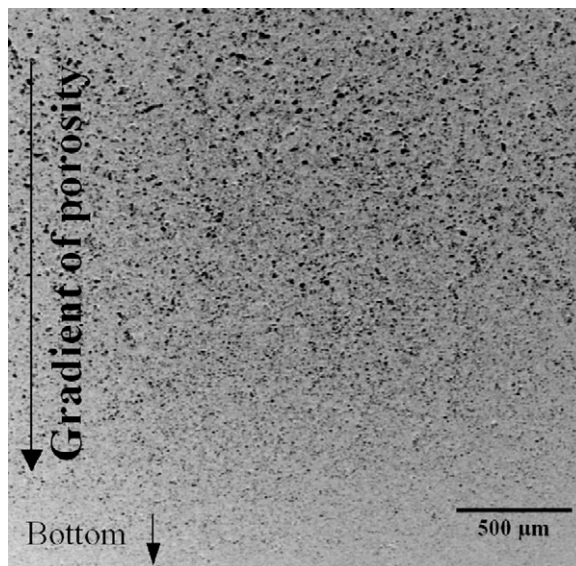

Fig. 2. Microstructure of a sintered sample from a powder compact obtained with a suspension height of 9.8 mm.

Fig. 3. Porosity and average pore diameter of sintered materials as a function of suspension height during centrifugation.

mine the intrinsic properties and 2000 nm so that the indented area takes into account the influence of pores. Two distinct directions, r and z, respectively, parallel and perpendicular to the direction of centrifugation were investigated in order to identify unexpected anisotropy of properties. The results presented thereafter correspond to a mean of 30–45 indents parallel and perpendicularly to centrifugation directions.

At the macroscopic scale, ultrasound immersion measurements were carried out at a frequency of 20 MHz to measure the Young's modulus in the r and z directions. The fracture strength of preliminary polished samples was measured by biaxial disc flexure using a piston on ring assembly.

3. Results

In Fig. 1, average densities of powder compacts against suspension height (8–15 mm) show that density increases continuously from $950\,kg\,m^{-3}$ (height = 8.4 mm) to $1280\,kg\,m^{-3}$ (height = 14.9 mm) while the thickness of the deposit ranges from 5.5 mm to 7.4 mm, respectively. After centrifugation, microstructures of powder compacts cannot be easily observed and were deduced from SEM observations of sintered compacts at 1300 °C. A typical microstructure is in Fig. 2 showing an increase of pore size from the bottom layer (container surface) to the upper layer (powder–liquid interface). A good correlation between Fig. 2 and microstructural characteristics of the initial powder compact is admitted since similar approach was used with different ceramic materials.[33,34] Consequently, a density gradient is assumed through the centrifuged powder deposit.

Analyses of SEM images from different sintered samples obtained with various suspension heights in the container give the total porosity and the average pore size in Fig. 3. The maximum value of total porosity is at 12–13 mm height and of average pore size at 10–11 mm height.

For quantitative texture analysis, the Rietveld fit firstly reveals that the only crystalline phase is (3:2) mullite (Fig. 4), which coexists with an amorphous phase. Considering that the amorphous phase is similar to amorphous silica, the fit quality is obtained with good reliability factors (Table 1). The refined cell parameters are similar to literature data.[35,36] The analyze of patterns obtained for 9.8 mm and 11.2 mm heights gives the {0 0 1}, {2 0 0} and {0 2 0} pole figures of Figs. 5–7, respectively. These
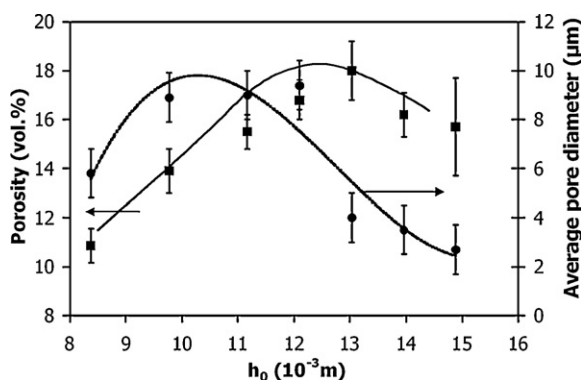
patterns illustrate the distributions of c-, a- and b-axes in samples. The fraction of texture components can be also observed from inverse pole figures of Fig. 8a and b. They are plotted for the main sample directions, r (ND), x (RD) and y (TD) for 9.8 mm (Fig. 8a) and 11.2 mm suspension height (Fig. 8b).
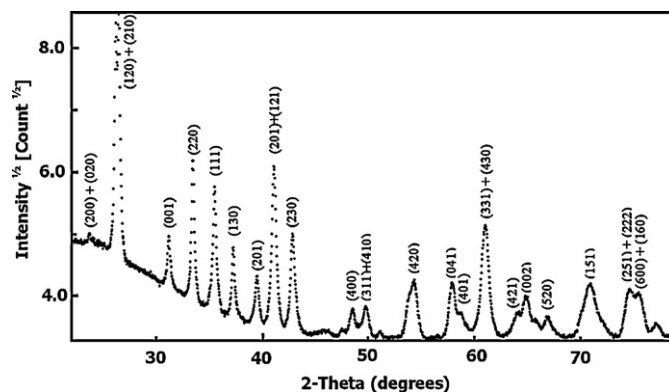

Fig. 4. X-ray diffraction pattern of the 11.2 mm sample. All the peaks are those of mullite.

Table 1
Reliability factors of samples 9.8 and 11.2 mm heights.

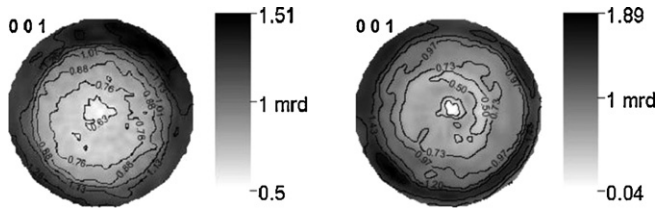| Suspension height	9.8 mm	11.2 mm
Rietveld fit		
R_w	12.0	19.6
R_B	9.6	15.6
Orientation distribution refinement		
R_w	5.7	14.7
R_B	5.6	11.6
Cell parameters		
a	7.51996 (6)	7.5237 (1)
b	7.66161 (5)	7.6610 (1)
c	2.87591 (1)	2.87563 (3)

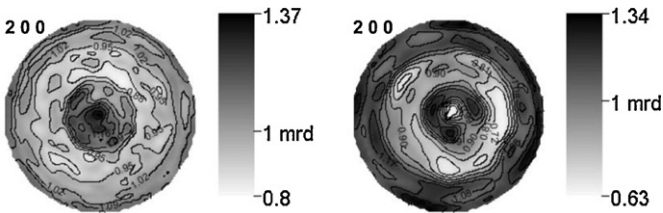Fig. 5. {0 0 1} pole figures of mullite of the 9.8 mm (left) and 11.2 mm (right) centrifuged samples.

Fig. 6. {2 0 0} pole figures of mullite for the centrifuged samples with 9.8 mm (left) and 11.2 mm heights (right).
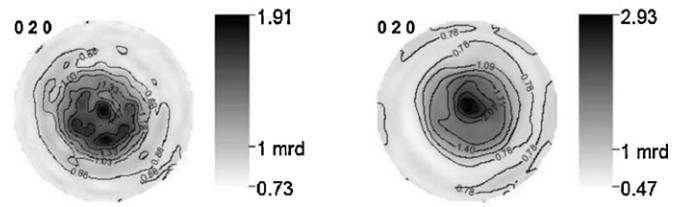

Fig. 7. {0 2 0} pole figures of mullite for the centrifuged samples with 9.8 mm (left) and 11.2 mm heights (right).
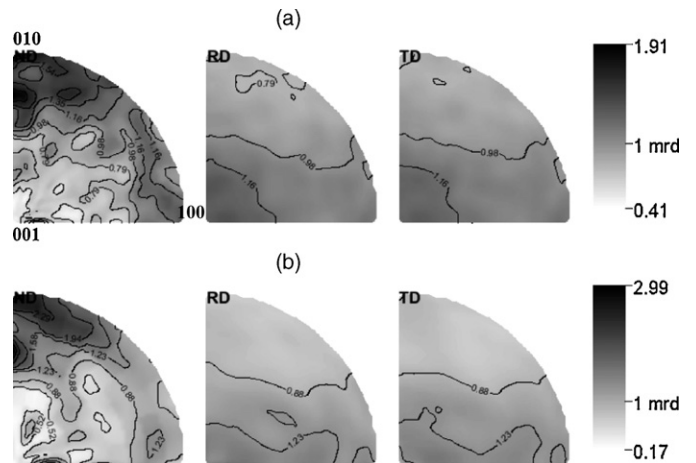

Fig. 8. Inverse pole figures for the centrifuged samples with (a) 9.8 mm and (b) 11.2 mm heights.

From SEM observations after chemical etching, microstructures of surfaces along r-axis and along z-axis of centrifugation are in Fig. 9a and b, respectively. We observe that the length of mullite crystals are in the range of 3–8 μm.

Young's modulus at the microscopic scale measured along r at a depth of 100 nm increases progressively with height from
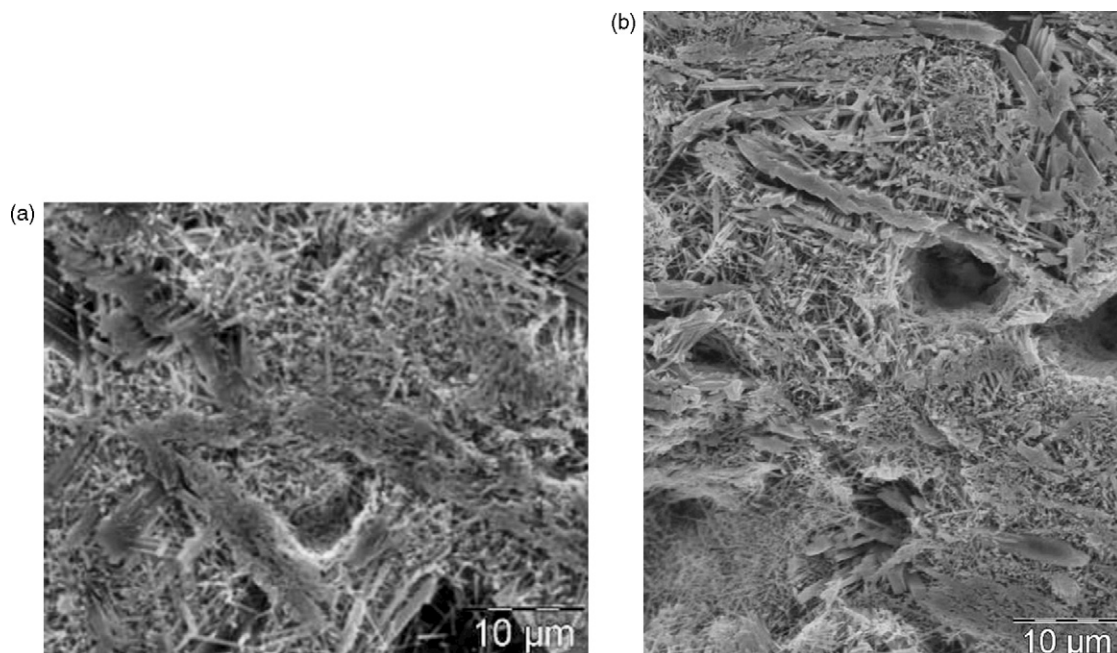

Fig. 9. Observation of mullite after chemical attack (a) along r-axis and (b) along z-axis to the centrifugation.
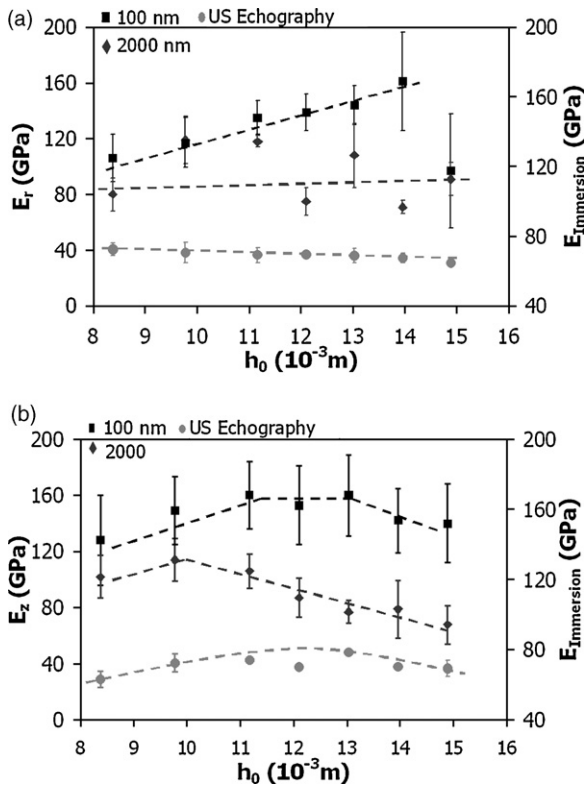
Fig. 10. Influence of the liquid height in the container of centrifugation on the Young's modulus: (a) E_r along the r-axis and (b) E_z along the z-axis. Measurement techniques are nano-indentation at 100 nm and 200 nm depths and immersion ultrasound.

8.4 mm to 14.9 mm (Fig. 10a). Along z, measurements show a maximum at 11.5–13 mm height (Fig. 10b). The comparison between Fig. 10a and b shows larger E_z than E_r below 13 mm height, indicating the specific role of suspension height into the container.

At the microscopic scale, Young's moduli were measured from nano-indentation technique at a depth of 2000 nm (Fig. 10a and b). Results present a significant standard deviation which is related to microstructural heterogeneity. Values are correlated to mean fracture stress along r, which present limited variation (Fig. 11).
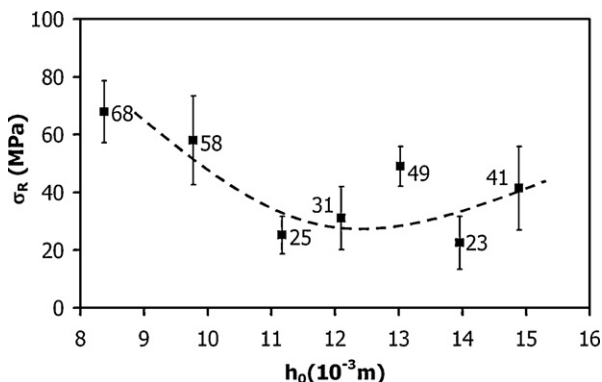

Fig. 11. Influence of the liquid height in the centrifugation container on the fracture strength (σ_R) measured by biaxial flexure.
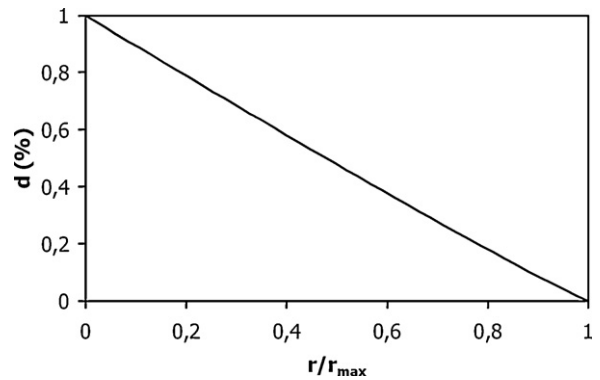

Fig. 12. Relative density of the powder compact through the section of the powder deposit.

4. Discussion

After centrifugation, experimental data of average density of the powder compact (Fig. 1) against the suspension height were used to calculate the n and β parameters of Eq. (1). Using these data, the calculated parameters are $\beta = 2870$ Pa and $n = 1.94$. Such a result supposes a continuous increase of density with the suspension height, but it differs from experiments since a density variation is observed in the microstructure of a sintered material (Fig. 2). Correlatively, the application of Eq. (2) in Fig. 12 illustrates a continuous decrease of density from the bottom to the liquid–solid interface.

The total porosity and the average pore size of materials have a maximum value for 12–13 mm height and 10–11 mm height, respectively (Fig. 3). From these data, we expect that the microstructural characteristics of the powder compact passes through an optimal value at intermediate suspension heights, whereas Eq. (1) supposes a continuous increase of density (Fig. 1).

Quantitative texture analysis of materials obtained at 9.8 mm and 11.2 mm heights, for {0 0 1}, {2 0 0} and {0 2 0} directions, give corresponding pole figures in Figs. 5–7. They illustrate the distributions of c-, a- and b-axes in samples. The {0 0 1} pole figures of the two materials exhibit c-axes mainly aligned parallel to, and at random, in the sample plane, as in a so-called "planar texture". The maximum orientation density is then located at the periphery of the {0 0 1} pole figures and reaches 1.5 m.r.d. and 2.1 m.r.d. for the 9.8 mm and 11.2 mm samples, respectively. The corresponding OD texture indexes are 1.16 m.r.d.[2] and 1.89 m.r.d.[2], revealing the overall weakly stabilized texture strength. The planar texture corresponds to the realignment of the c-axes perpendicularly to the pressure direction of centrifugation r. A small tilt angle is seen with the orientation density at the periphery of the {0 0 1} pole figures, but mainly for the 9.8 mm sample. It is from the settling direction during centrifugation, which is not exactly oriented perpendicularly to the bottom of centrifugation containers. Most importantly, the minimum value of the {0 0 1} pole figures indicates that nearly 50% of the volume of the 9.8 mm sample is not oriented within the planar texture component, while for the 11.2 mm sample, only 4% are not in this component.

Table 2
Influence of the porosity v (%) on the intrinsic Young's modulus of the dense material along r and z directions.

h_0 (mm)	8.4	9.8	11.2	12.1	13.0	14.0	14.9
v (%)	10.9 (0.1)	14.9 (0.9)	14.5 (0.7)	16.8 (0.8)	18.0 (1.2)	16.2 (0.9)	15.7 (2.0)
E_0 (r)	98	104	100	109	112	103	97
E_0 (z)	85	107	107	109	127	107	104

Around the *c*-axes, all other crystallographic directions are randomly distributed in the planar texture. Consequently, a broad maximum should be observed in the center of any $\{h\,k\,0\}$ pole figure, like $\{0\,2\,0\}$ (Fig. 6), with a maximum of 1.9 m.r.d. for the 9.8 mm sample and 2.9 m.r.d. for the 11.2 mm sample. However, the $\{2\,0\,0\}$ pole figures (Fig. 7) does not fully respect this scheme, but exhibits a reinforcement of their equators, superposed to the planar component of their center. This is coherent with the existence of a second texture component, corresponding to a $\langle 0\,1\,0 \rangle$ fibre-like texture. This latter component increases with the initial suspension height, as denoted both by the maximum density increase of the $\{0\,2\,0\}$ pole figure center and by the equator density increase on the $\{2\,0\,0\}$ pole figure. Furthermore, slight reinforcements are visible along the equator of this latter. Such inhomogeneity of density levels along the equatorial ring corresponds to a tendency towards alignment of the *a*-axes in the sample plane. Roughly, four reinforcements are visible, defining two directions for alignment in the plane, at 90° from each other.

The proportion of each of the texture components is also discussed on inverse pole figures (Fig. 8) plotted for the main sample directions, *r* (ND), *x* (RD) and *y* (TD).

In the radial inverse pole figures, one can clearly see that the broad periphery in the 9.8 mm sample (Fig. 8a), disappears in the 11.2 mm sample (Fig. 8b) to restrict near the $\langle 0\,1\,0 \rangle$ directions. Simultaneously, the relatively strong $\langle 0\,0\,1 \rangle$ direction pole observed on the *x* and *y* pole figures in 9.8 mm transforms into a quite perfectly homogeneous density in $\langle 0\,0\,1 \rangle$ but mainly in the $\langle 1\,0\,0 \rangle$ directions of the 11.2 mm material. The planar texture component then clearly becomes minor and the fibre component with *b*-axes of mullite aligned parallel to *r*, becomes the major component of the 11.2 mm sample. This component evolution is operated at the expense of the randomly oriented crystals, which is up to 41% of the sample volume for 9.8 mm and decreases to only 17% for 11.2 mm.

All QTA results show that centrifugation process exhibits good capabilities to orient mullite in materials from clay minerals suspensions. A careful monitoring of the suspension height allows achieving an optimized, though moderating texturation of the mullite crystals. 96% of the material volume contains mullite with one planar texture component.

Mechanical characterization indicates the occurrence of a significant anisotropy between *r* direction (Fig. 10a) and *z* direction (Fig. 10b). Its extend is mostly related to parameters used during the centrifugation process and to the suspension height into the container. When the liquid height increases from 8.4 mm to 14.9 mm, the Young's modulus measured at a depth of 100 nm along *r* increases progressively. The comparison between Fig. 10a and b shows that until 13 mm, the E_z values are

larger than that of E_r, but for 14 and 14.9 mm, anisotropy vanishes. The difference between Young's modulus measured along *r* and *z* axes is correlated to the orientation of mullite, since it is also evidenced by QTA. The more significant difference at 11.2 mm height is related to a more organized texture.

At a larger scale (2000 nm indentation depth), similar variations are observed with a maximum value of E_z at about 10 mm height (Fig. 10b) and a slight increase of E_r with height (Fig. 10a). In general, 2000 mm values are below 100 nm values, which should be related to microstructural characteristics and mainly porosity. The decrease of E with larger sample volume for the measurement is also observed when macroscopic E is measured by US echography technique, which has lowest values in either the *r* and *z* directions (Fig. 10a and b). It is seen that all microstructural components, i.e. porosity and different phases, contribute to the macroscopic E.

Global information is also obtained with biaxial flexure strength σ_R in Fig. 11, which decreases when height increases. This trend is related to the probability to find more critical defects when sample volume increases with the initial suspension height. The decrease of σ_R cannot be predominantly correlated to porosity (Table 2) because its variation with the suspension height is limited and therefore the orientation degree of mullite is supposed to have a significant influence on σ_R values. Particularly, σ_R measured for a height of 11.2 mm is close to minimum (Fig. 11). Since this result was obtained in the direction perpendicular (*r*-axis) to the expected direction of mullite, it also supposes a preferential orientation. It can be thought that weak σ_R values are related to relatively high Young's modulus, but also to significant anisotropy between *r* and *z* values (Fig. 10a and b). The preferential orientation of mullite perpendicularly to the direction of biaxial flexure load weakens significantly the mechanical properties in this direction.

The role of porosity in mechanical properties was investigated since an increase of porosity must lead to a decrease of fracture strength and Young's modulus. The relationship between E and porosity v can be described using the equation[37]:

$$E_0 = \frac{E_{\exp}}{\exp(-p.v/1-v)} \tag{3}$$

where E_0 is the intrinsic Young's modulus of the dense material (without porosity) and p is an empirical parameter equal to 2.2.[37] The value of $E_0(r)$ and $E_0(z)$ were calculated using $E_{\exp}(z)$ that is macroscopic Young's modulus E_r (Fig. 10a) and E_z (Fig. 10b) measured by US echography.

In Table 2, the limited variation of calculated $E_0(r)$ and $E_0(z)$ against suspension height is evidenced. For 13 mm height, $E_0(r)$ and $E_0(z)$ as $E_0(r) - E_0(z)$ present maximum values, whereas porosity increases up to 13 mm and then decreases slightly. A

similar tendency is observed in Fig. 10a and b with E_r and E_z measured by nano-indentation at 100 nm depth. Therefore, we assume that intrinsic Young's modulus is not correlated highly correlated to porosity, which suggests the key role of mullite orientation degree.

Whereas correlation between mechanical properties and orientation of mullite is observed, which weaken the strength in r direction, the limited values of fracture strength is related to the small size of mullite. SEM observations of Fig. 9a and b show that mullite length is in the range 2–10 μm (diameter 0.2–0.3 μm) and has a wide distribution of sizes. Crystals are preferentially oriented in r direction, but within distinct and non-contiguous domains. To further increase both size and orientation degree, it will be necessary to study in details the effect of thermal treatments and specific additives.

5. Conclusion

In this study, the centrifugation process of kaolinite suspensions has been optimized by identifying the key parameters of process, that is mostly the suspension height into centrifugation containers. The mechanical properties of sintered materials are influenced by both the porosity and the microstructural characteristics. But the orientation of mullite appears to be predominant since Young's modulus related to anisotropy of the bulk material exhibit maximum values although porosity varies significantly. Beside, mechanical properties are also correlated to mullite distribution by quantitative texture analysis since the OD texture index attains 1.89 m.r.d.^{2} for 11.2 mm suspension height, indicating the existence of a stabilized texture strength. It evidences a planar texture where only 4% of the volume of the 11.2 mm sample is not oriented within the planar texture component.

To improve the orientation of mullite in microstructures, future ways can be investigated as using an alternative shaping process such as tape casting or adding template particles.

Acknowledgements

References

1. Lee S-H, Lee Y-I, Kim Y-W, Xie R-J, Mitomo M, Zhan G-D. Mechanical properties of hot-forged silicon carbide ceramics. *Scr Mater* 2005;**52**:153–6.
2. Baldacim SA, Santos C, Silva OMM, Silva CRM. Mechanical properties evaluation of hot-pressed Si₃N₄–SiC$_{(w)}$ composites. *Int J Refract Metals Hard Mater* 2003;**21**:233–9.
3. Habelitz S, Carl G, Rüssel C. Processing, microstructure and mechanical properties of extruded mica glass–ceramics. *Mater Sci Eng* 2001;**A307**:1–14.
4. Granahan M, Holmes M, Schulze WA, Newnham RE. Grain-oriented PbNb₂O₆ ceramics. *Commun Am Ceram Soc* 1981:C68–9.
5. Hong S-H, Messing GL. Development of textured mullite by templated grain growth. *J Am Ceram Soc* 1999;**82**(4):867–72.
6. Tohru S, Suzuki T, Uchikoshi H, Okuyama Y, Sakka K. Mechanical properties of textured, multilayered alumina produced using electrophoretic deposition in a strong magnetic field. *J Eur Ceram Soc* 2006;**26**(4–5):661–5.
7. Dong-Kyu K, Waltraud M. Oxide laminated composites with aluminum phosphate (AlPO₄) and alumina platelets as crack deflecting materials. *Compos: Part B* 2006;**20**:1–6.
8. Gridi-Bennadji F, Chateigner D, Di Vita G, Blanchart P. Mechanical properties of textured ceramics from muscovite–kaolinite alternate layers. *J Eur Ceram Soc* 2009;**29**(11):2177–84.
9. Taruta S, Fujisawa R, Kitajima K. Preparation and mechanical properties of machinable alumina/mica composites. *J Eur Ceram Soc* 2006;**26**(9):1687–93.
10. Watts J, Hilmas G. Crack deflection in tungsten carbide based laminates. *Int J Refract Metals Hard Mater* 2006;**24**:222–8.
11. Guilmeau E, Itahara H, Tani T, Chateigner D, Grebille D. Quantitative texture analysis of grain-aligned [Ca₂CoO₃]₀.₆₂[CoO₂] ceramics processed by the reactive-templated grain growth method. *J Appl Phys* 2005;**97**:0649021–7.
12. Messing GL, Trolier-McKinstry S, Sabolsky EM, Duran C, Kwon S, Brahmaroutu B, et al. Templated grain growth of textured piezoelectric ceramics. *Crit Rev Solid State Mater Sci* 2004;**29**(2):45–96.
13. Castelein O, Guinebretière R, Bonnet JP, Blanchart P. Shape, size and composition of mullite nanocrystals from a rapidly sintered kaolin. *J Eur Ceram Soc* 2001;**21**(13):2369–76.
14. Gridi-Bennadji F, Beneu B, Laval JP, Blanchart P. Structural transformations of muscovite at high-temperature by X-ray and neutron diffraction. *Appl Clay Sci* 2008;**38**(3–4):259–67.
15. Lee WE, Souza GP, McConville CJ, Tarvornpanich T, Iqbal Y. Mullite formation in clays and clay-derived vitreous ceramics. *J Eur Ceram Soc* 2008;**28**(2):465–71.
16. Soro N, Aldon L, Jumas JC, Blanchart P. Iron role on mullite from kaolin by Mössbauer spectroscopy and Rietveld simulation. *J Am Ceram Soc* 2003;**86**(1):129–34.
17. Pialy P, Tessier-Doyen N, Njopwouo D, Bonnet JP. Effects of densification and mullitization on the evolution of the elastic properties of a clay based material during firing. *J Eur Ceram Soc* 2009;**29**(9):1579–86.
18. Schneider H, Eberhard E. Thermal expansion of mullite. *J Am Ceram Soc* 1990;**73**(7):2073–6.
19. Carbajal L, Rubio-Marcos F, Bengochea MA, Fernandez JF. Properties related phase evolution in porcelain ceramics. *J Eur Ceram Soc* 2007;**27**(13–15):4065–9.
20. Tucci A, Esposito L, Malmusi L, Rambaldi E. New body mixes for porcelain stoneware tiles with improved mechanical characteristics. *J Eur Ceram Soc* 2007;**27**(2–3):1875–81.
21. Ece OI, Nakagawa Z-E. Bending strength of porcelains. *Ceram Int* 2002;**28**(2):131–40.
22. Bragança SR, Bergmann CP. A view of whitewares mechanical strength and microstructure. *Ceram Int* 2003;**29**(7):801–6.
23. Amoros JL, Orts MJ, García-Ten J, Gozalbo A, Sanchez E. Effect of the green porous texture on porcelain tile properties. *J Eur Ceram Soc* 2007;**27**(5):2295–301.
24. Moon RJ, Hoffman M, Hilden J, Bowman KJ, Trumble KP, Rödel J. R-curve behavior in alumina–zirconia composites with repeating graded layers. *Eng Fract Mech* 2002;**69**(September (14–1)):1647–65.
25. Moon RJ, Hoffman M, Bowman KJ, Trumble K. Layer orientation effects on the R-curve behavior of multilayered alumina–zirconia composites. *Compos B: Eng* 2006;**37**(6):449–58.
26. Shih W-H, Kim SI, Shih WY, Schilling CH, Aksay IA. Consolidation of colloidal suspensions. *Mater Res Soc Symp Proc* 1990;**180**:167–72.
27. Moon RJ, Bowman KJ, Trumble KP, Rödel J. Fracture resistance curve behavior of multilayered alumina–zirconia composites produced by centrifugation. *Acta Mater* 2001;**49**(6):995–1003.
28. Chateigner D, editor. *Combined analysis: structure–texture-microstructure-phase-stresses—reflectivity analysis by X-ray and neutron scattering*. 2004. p. 152p, www.ecole.ensicaen.fr/~chateign/texture/combined.pdf.

29. Lutterotti L, Chateigner D, Ferrari S, Ricote J. Texture, residual stress and structural analysis of thin films using a combined X-ray analysis. *Thin Solid Films* 2004;**450**(1):34–41.

30. Chateigner D. Reliability criteria in quantitative texture analysis with experimental and simulated orientation distributions. *J Appl Crystallogr* 2005;**38**(4):603–11.

31. Oliver WC, Pharr GM. An improved technique for determining hardness and elastic modulus using load and displacement sensing indentation experiments. *J Mater Res* 1992;**7**(6):1564–83.

32. Oliver WC, Pharr GM. Measurement of hardness and elastic modulus by instrumented indentation: Advances in understanding and refinements to methodology. *J Mater Res* 2004;**19**(1):3–20.

33. Hotta T, Abe H, Naito M, Takahashi M, Uematsu K, Kato Z. Effect of coarse particles on the strength of alumina made by slip casting. *Powder Technol* 2005;**149**(2–3):106–11.

34. Abe H, Naito M, Hotta T, Kamiya H, Uematsu K. Pore defects related to slurry character and their relevance to strength distribution in alumina ceramics. *Powder Technol* 2003;**134**(1–2):58–64.

35. Fischer RX, Schmucker M, Angerer P, Schneider H. Crystal structures of Na and K aluminate mullites. *Am Mineral* 2001;**86**(11–12):1513–8.

36. Crystallography Open Database no. 9005501. www.crystallography.net.

37. Pabst W, Gregorova E, Ticha G. Elasticity of porous ceramics—a critical study of modulus–porosity relations. *J Eur Ceram Soc* 2006;**26**(7):1085–97.